# Microfocus spectroscopy experiments on mineral deposits and in cultural heritage science at Diamond Light Source.

*Josep Roque-Rosell[1], Joaquin Proenza[2], Nicholas Estaugh[3] Marius Vendrell-Saz[2], and Fred Mosselmans[1]*

[1] Diamond Light Source Ltd, Chilton, Didcot, OX11 0DE, UK

[2] Departament de Cristal.lografia Mineralogia i Diposits Minerals, Universitat de Barcelona, Barcelona, 08028, SPAIN.

[3] RLAHA, Perrins Building, South Parks Road, Oford,OX1 3QY, UK

**Abstract**

Third generation synchrotrons allowed to perform experiments which had a major impact in the field of environmental science and related disciplines such as mineralogy and cultural heritage. This paper presents some basic concepts on synchrotron radiation and the fundamentals of X-ray absorption fine spectroscopy — XAFS —are introduced and accompaigned with three examples on cultural heritage and mineralogy with the aim to show the opportunities those XAFS techniques provide. The first example is the study lustre ceramics found in an archaeological site in Paterna to elucidate how they were produced, the second example is related to the systematic study of vermillion pigments from across Europe and Asia to target possible useful trace elements involved in their decay, and finally a third example is shown related to the study of a mineralogical problem aiming to understand the speciation and association of Ni in a laterite from Moa Bay (Cuba) where the sorption of Ni on Mn oxyhydroxides is taking place.

**Introduction**

Synchrotrons facilities provide new opportunities to perform novel scientific experiments that couldn't have been achieved with classical X-ray sources such as X-ray tubes (*Widemann 2003*). Synchrotron radiation provides a continuum ultraviolet and

X-ray radiation five to ten orders of magnitude brighter than that from sealed or rotating-anode X-ray tubes (*Beran and Libowtzky 2004*). Although the absortpiton of X-rays by matter had been observed previously and provided promising results, it wasn't until that the development of the synchrotron sources that allowed establishing the X-ray Absorption Fine Spectroscopy — XAFS, including Extended X-rays Absorption Fine Structures EXAFS and X-ray Absorption Near the Edge Structures XANES domains — as useful and powerful technique to obtain information on the local and medium range structural order around a chemical element in condensed matter (solids, liquids, interfaces, etc…). XAFS is an element specific technique that allows determining the structure of the local environment of an atom — however is neither simple nor straightforward in interpretation.

**Basic concepts on synchrotron radiation**

Synchrotron radiation is based on the fact that high energy electrons traveling in a circular orbit close to the speed of light emit electromagnetic radiation tangential to their orbit and the emitted radiation and the subsequent electromagnetic waves interfere providing continuous wide range energies. The facilities that accelerate the electrons and keep them in orbit are called synchrotrons, and usually consist in a doughnut shaped buildings containing a radiation shielded storage ring and beamlines that are tangentially placed around it as seen on Figure 1. To generate the synchrotron light "bunches" of electrons are injected in a circular accelerator called booster by means of a linear accelerator. Bunches of electrons can orbit around the storage ring and a numerous bunches of electrons can be grouped together into a "train" of bunches and then transferred from the booster synchrotron to the storage ring where they are kept running and producing synchrotron radiation.

A typical storage ring comprises symmetric straight and bending sections of stainless steel tubes under ultra high vacuum with a set of complex magnetic devices to focus the electron bunches and bend their path and keeping them in a determined orbit. To produce the synchrotron radiation a normal acceleration is applied to the electron bunches by means of bending magnets (BM) and insertion devices (ID). BM are big dipole magnets installed in the curved sections of the ring, instead the ID, known as

wigglers and undulators, are designed and inserted in the straight sections of the storage ring and are mainly constituted by an array of oriented dipole magnets arranged in a way that as the electron bunches pass through their trajectory oscillate sinusoidally in the horizontal plane as seen on Figure 2.

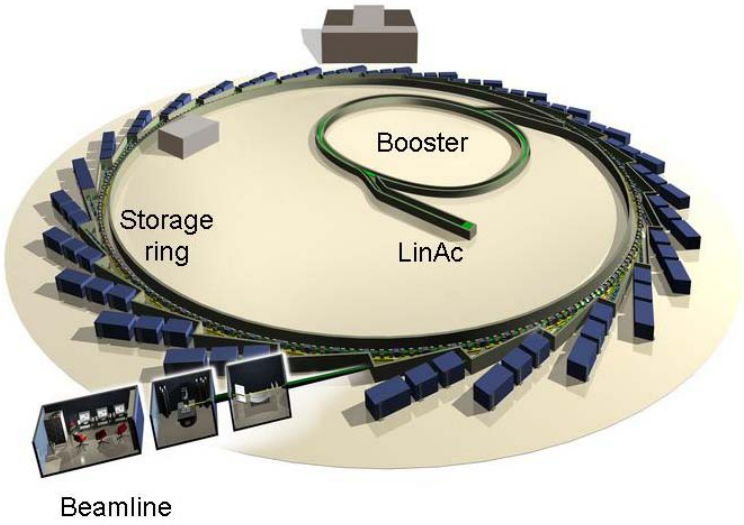


*Figure 1 3D scheme of a sycnchortron facilities showing the linear accelerator, the booster, the storage ring, the beamlines (with their optics, experimental and the control panel hutches).*

The ID is called wiggler when the radiation resulting from each individual set of poles incoherently superimposes with the radiation from all the other poles, and it is called undulator when the radiation resulting from each dipole pair is coherently superimposed and the radiation constructively and destructively interferes producing a narrower emission cone as seen on Figure 2. The main difference between wigglers and undulators reside in fewer dipole magnets in wigglers, resulting in a continuous spectrum with a higher flux and a spectrum that extends to shorter wavelengths than bending magnets. The beamlines are the windows in the storage ring that collect and focus the photons provided by BM and ID on the sample. Usually they are constituted by a front end, the beamline optics, the experimental station and optionally a control

panel. The beamline optics usually involves a set of optical elements such apertures, slits, mirrors and monochromators with the objective to deliver photons with the desired spatial resolution, energy resolution and spectral brightness.

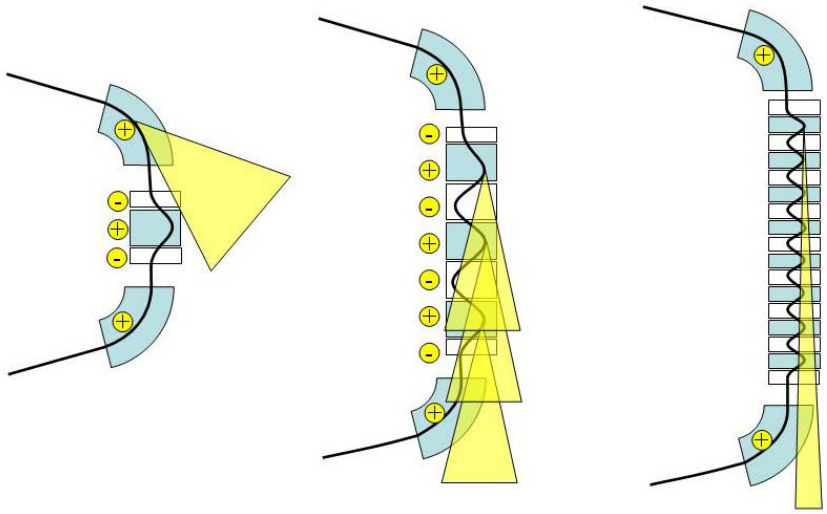

*Figure 2 Synchrotron radiation sources from left to right (a) bending magnet with the resulting radiation fan (b) multipole wiggler device showing a radiation cone as the sum flux of the magnetic poles and finally (c) undulator device showing a radiation cone resulting from the interference between different dipole emissions. Courtesy of Diamond Light Source Ltd.*

The microfocussing beamlines providing a micrometric beam spot (from 10 μm down to 1 μm) are from special relevance when studying geological and cultural heritage related materials which are heterogeneous in nature. At the end of the beamline the experimental stations are built with detectors and movable stages to take advantage of the photons the source and the beamline optics can provide.

**I18 from Diamond Light Source**

The third generation synchrotrons have smaller source sizes and low that combined with advances in hard X-ray optics (Howells et al. 2000*)* has led to the development of a great number of hard X-ray microprobe beamlines that had a big impact on environmental science in the last 10 years (e.g. Martinez et al. 2006). The I18

is the Diamond Light Source (DLS) microfocus spectroscopy beamline that operates with a range of energy from 2-20 keV allowing scanning the K-edges of the elements from P through to Mo and the L-edges from Mo to Pu. This beamline shown on Figure 3 can perform XAS on ~85% of the natural elements in the periodic table and is specially suited to perform studies in environmental and earth science i.e. to study fluid inclusions, mining, toxic metal speciation, bioremediation, transport mechanisms, radioactive waste disposal, climate indicators, archaeometry and extraterrestrial geology.

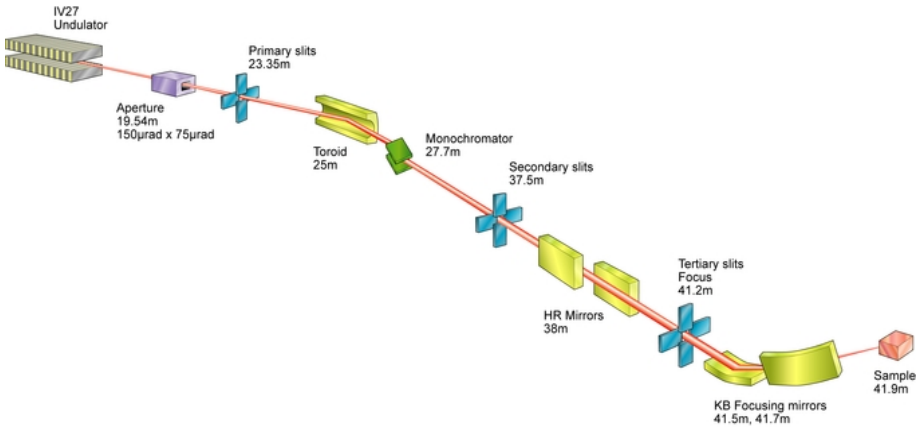


*Figure 3 Beamline layout designed for micron X-ray Absorption Spectroscopy for the study of complex inhomogeneous materials. It has a wide range of applications where structural and chemical information at micron level is required. Courtesy of Diamond Light Source.*

*Beamline optics*

The optical scheme of I18 is based on three mirrors and a liquid nitrogen-cooled double crystal monochromator. The first device, at 25 m from the source, is a water-cooled Rh-coated Silicon toroidal mirror that focuses the beam in the horizontal plane at 37.5 m from the source, and collimates it in the vertical direction. Next is the fixed-exit monochromator which has two sets of crystals available Si(111) and Si(311). The angular range of the monochromator is such that it can cover from 2 – 20 keV on the Si(111) set, and the Si(311) can be used to obtain better resolution from above 15 keV. The last two pairs of mirrors are in the experimental hutch. First there is a pair of

plane mirrors, which will be used for harmonic rejection that are set at an angle low enough to absorb all but the primary beam off the monochromator. The use of a pair of mirrors keeps the photon beam in the same position regardless of that angle with two stripes for use at various energies — Rh and Ni. Finally there are the Kirkpatrick-Baez focusing mirrors mechanically bended to obtain a focussed beam down to ~ 3×3 μm. These are non-chromatic and can be used for energy scanning applications — explained below — and operate over the full beamline energy range, using three stripes, Cr, Pt and Pd (Mosselmans et al. 2008).

*Experimental set-up*

The measurements take place at the end-station on Figure 4 . The sample holder uses a magnetic sample mount which sits on a 7-axis Newport-Microcontrole sample stage. The stage allows the positioning of the sample to 100 nm resolution by moving along three vertical axes and two normal horizontal axes and with fine θ axis which can be used to study samples using fluorescence micro-tomography. The stage rasters the sample in front of the X-ray beam to give micro μ-XRF maps and by changing the energy of the incident beam information about the valence state and speciation in addition to elemental composition is obtained.

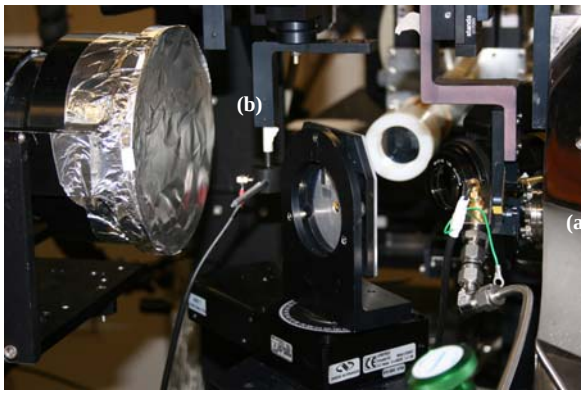


*Figure 4 The I18 end-station showing the (a) Ortec detector, (b) the Photonics Science CCD, (c) the rotary stage, the (d) the micro-ion chamber with flowing He and (e) the optical microscope. The sample stage is rotated 45$^{o}$ facing to the Ortec detector for fluorescence experiments.*

The beamline is equipped with two energy-resolving fluorescence detectors to cover the energy range of the beamline. The first is an Ortec 9-element monolithic Ge detector with XSPRESS2 electronics effective for X-rays with energies > 3.5 keV. To cover the lower range of energies a four elements Sii- Nanotechnology Vortex Si Drifts detector which can detect X-rays with energies >1 keV is used. The two detectors are situated on different sides of the sample stage. Combined with the fluorescence a detector there is a Photonic Science VHR CCD camera to collect diffraction data in transmission geometry, with a maximum 2θ of ~50$^{o}$. Beam monitoring is normally performed with a Repic Co. micro-ion chamber used with flowing He, however a drain current option is available for work at low energies. The end station is shown in Figure 4. A range of standard sample environments is available on the beamline including a vacuum or He electron yield cell and two Linkam stages that cover the temperature range 100-1500 K.

**X-ray absorption Spectroscopy**

When the X-rays photons interact with matter the photoelectric effect induce an absorption edge when the incoming energy of the X-rays correspond to the binding energy of electrons in atomic core levels — *1s*, *2s*, etc... When the photon is absorbed promotes a core level electron (*K*, *L*, or *M* shell) out of the atom and the atom is left in an excited state with an empty electronic level. The electron ejected is called photoelectron and is emitted as an outgoing wave that is backscattered by the surrounding atoms, giving an interference signal as shown on Figure 5.

The X-ray absorption is determined by the Beer-Lambert law in eq. 1

$$\mu x = \ln\left(I_0 / I\right) \quad \text{(eq. 1)}$$

Where the $I_0$ and $I$ correspond to the intensity of the incident and transmitted beam respectively, $x$ is the thickness of the sample and $\mu$ the absorption coefficient that depends on the incident X-ray energy. The $\mu$ decreases smoothly with increasing the X-rays photon energy, and exhibits discontinuities which constitute the absorption edges. Near the absorption edge transitions to bound states may be observed such as the

so called “pre-edge” that can be observed on the low energy side of the absorption *K* edge of transition elements. This is characteristically associated to transition on partly empty *d* states.

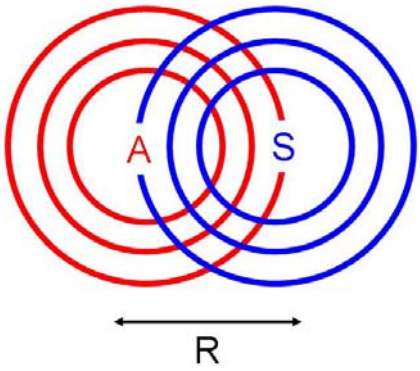


*Figure 5 The photoelectron wave emitted in red from the absorbing atom A is backscattered by a neighbouring scattering atom S in blue. The backscattered wave modifies the final-state wave function at the absorber. The emitted and scattered waves interfere constructively or destructively depending on their out of phase. R corresponds to the interatomic distance.*

The value of the energy of a the absorption edge for a given element $E_0$ can vary as much as $\pm$ 10 eV because of modifications of the local electronic structure linked to the environment and the oxidation state of the absorbing element . The EXAFS part of the spectrum corresponds to the modulation of the X-ray absorption coefficient related to the backscattered electron waves at photon energies above $E_0$ — from 50 eV to 1000 eV above the edge. By the other hand the absorption features observed in the edge region correspond to the XANES as seen on Figure 3.

**Simple description of EXAFS theory**

In EXAFS the photoelectron is regarded as a free single electron that produces the oscillations. In a wide range of systems only simple scattering process are considered but in crystalline systems the so called multiple scattering effect can be important. An example of X-ray absorption spectrum is shown on Figure 6 at the Ti K-

edge from $EuTiO_3$. The absorption edge is due to a Ti *1s* core level electron ejected to the continuum.

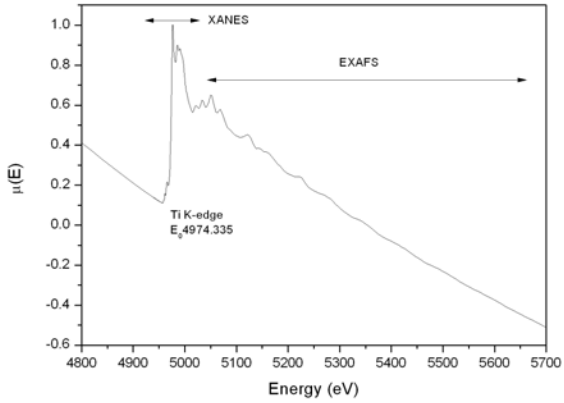


*Figure 6 XAFS spectrum of Ti at the Ti* K*-edge in EuTiO3 showing the XANES and EXAFS domains.*

After the edge the EXAFS oscillations are described as a sum of sine waves with a modulation coefficient $\chi(E)$ given by eq .2

$$\chi(E) = \frac{\mu(E) - \mu_0(E)}{\mu_0(E)} \text{ (eq. 2)}$$

where $\mu(E)$ is the measured absorption coefficient and $\mu_0(E)$ corresponds to the absorption of an isolated atom used as a background. When the difference between the two coefficients is normalized by $\mu_0(E)$ — which is proportional to the amount of atoms per volume — normalises the EXAFS to an atom basis. The $\chi(E)$ is linked to the structural parameters by converting the X-ray energy $E$ into a wave-number $k$ defined in eq. 3

$$k = \left( \frac{2m(E - E_0)}{\eta^2} \right)^{\frac{1}{2}} = \left(0.262(E - E_0)\right)^{\frac{1}{2}} \text{ (eq. 3)}$$

where $E_0$ is the absorption edge energy, $m$ is the electron mass and $\eta$ corresponds to the reduced Plank constant. By converting the X-ray energy to the wave-number of the photoelectron $k$, which is a space analogy to time frequency and has dimensions 1/distance, the EXAFS oscillations are then defined by $\chi(k)$. The oscillations as function of photo-electron wave number and $\chi(k)$ is often referred to simply as the EXAFS itself.

The different frequencies present in the $\chi(k)$ oscillations correspond to different near atom coordination shells which can be described and modeled according to the EXAFS in eq. 4

$$\chi(k) = \sum_j \frac{N_j f_j(k) e^{-2k^2\sigma_j^2} e^{-2R_j/\lambda(k)}}{kR_j^2} \sin(2kR_j + \delta_j(k)) \quad \text{(eq. 4)}$$

where the index $j$ refers to the atomic shell, $R$ is the distance between the absorbing atom and the neighbouring atom in the $j^{th}$ shell, $\delta(k)$ is a phase function related to both central and backscattering atoms, $N$ is the number of neighbouring atoms, $f(k)$ the backscattering amplitude function corresponding to the atomic species on this shell, $\sigma^2$ the disorder in the neighbour distance and $\lambda(k)$ is the mean free path length of the photoelectron. It should be notice that since the scattering factors depend on the Z of the neighbouring atom EXAFS is also sensitive to the atomic species of the surrounding atoms.

**Data collection**

The XAFS experiments need an accurate measurement of $\mu(E)$ since XAFS correspond to a small part of the total absorption. Errors in the measurement of $\mu(E)$ can degrade and distort the XAFS. The X-rays generated from the synchrotron source

are scanned in the range of energies interested in the sample. Measurements for the $I_0$ and the $I_t$ in transmission measurements are performed by means of ion-chambers — parallel capacitor filled with an inert gas and with a high voltage across through the X-ray beam passes — instead for fluorescence measurements several types of detectors can be used i.e. germanium solid state and silicon drift detectors as shown in Figure 7.

For concentrated samples where the element of interest is a major component, XAFS should be measured in transmission. To do this, we need enough transmission through the sample. The sample thickness $x$ should be adjusted so that $\mu x \approx 2.5$ above the absorption edge and/or the edge step $\Delta\mu(E)x \approx 1$. Jus to give an idea for metals thickness is in several micron range to tens of microns. For diluted samples however sample thickness are about the millimetre range. In transmission measurements the sample should be uniform and free of pinholes. For a powder the grain size shouldn't be bigger than an absorption length.

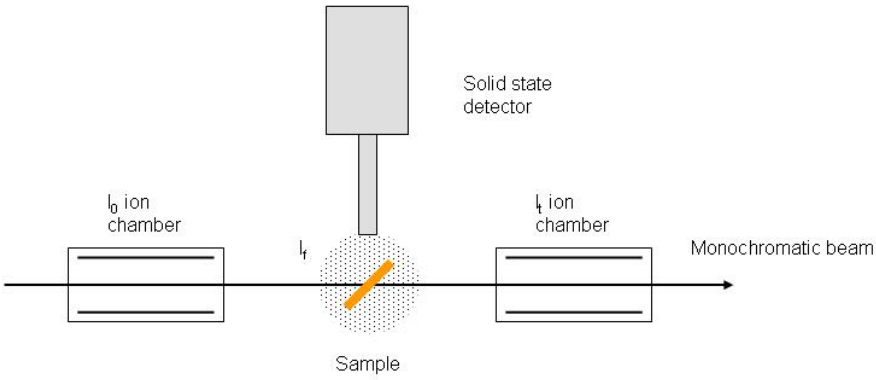


*Figure 7 Beamline set up for an X-ray absorption experiment showing the ion chambers to measure the amount of absorbed beam when scanning on a range of energies on the sample and the solid state detector to perform measurements in a fluorescence geometry.*

For thick samples or lower concentrations — down to the ppm level — performing the experiments in fluorescence geometry is needed. In fluorescence XAFS the X-rays emitted from the sample will include the fluorescent line of interest, the fluorescence lines from other elements in the samples and scattered X-rays (Compton

peak). Figure 8 shows fluorescence lines from Cr, Mn, Fe, Co and Ni from a soil sample. Thus energy discrimination is important to suppress the scatter peak and other fluorescence lines, and collect only the intensity of the lines of interest. Energy discrimination can be done by filtering the non desired emissions before it gets to the detector or done electronically after it is detected.

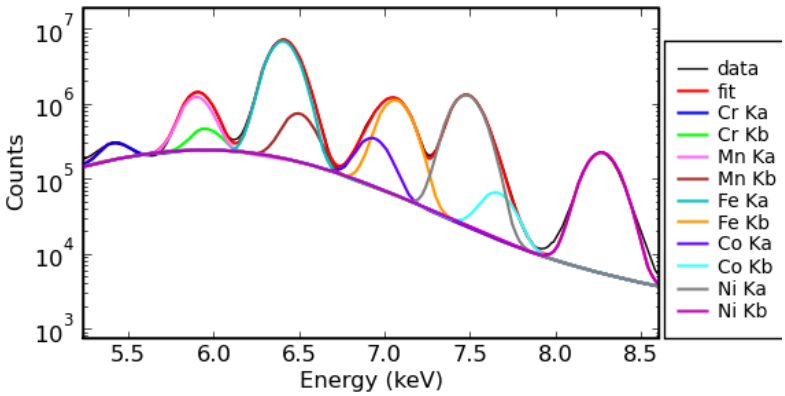


*Figure 8. Spectrum showing the fluorescence lines from a soil sample obtained with a 9 elements Ge detector. The selected element is windowed electronically from the spectrum to measure its absorption.*

Physically filtering can be performed by placing a Z-1 rich material between the sample with the element of interest Z and the fluorescence detector. Due to the absorption edge the filter will above the scatter peak and pass the line of interest suppressing the background intensity and increase the signal to noise level. Electronically the solid state Si and Ge detectors can achieve energy resolution of ~ 150 eV and able to measure the full fluorescence spectra and then select the unwanted portions windowing only the fluorescence lines of interest. In XAFS experiments the measured $\mu(E)$ data is reduced to obtain $\chi(k)$ and then is analyzed using the XAFS equation eq. 4.

When performing fluorescence experiments the self-absorption effect should be taken into account. In fluorescence photons have a lower energy than the corresponding

edge, and so are not absorbed by the element of interest, however as the energy is scanned during an EXAFS the variation in sample absorption causes variations in the penetration depth of the incident X-rays, which therefore affects the fluorescence yield. As absorption increases — increasing the fluorescence yield — the penetration depth decreases — reducing the fluorescence yield — and therefore dampening the change in absorption observed by fluorescence. The self-absorption implies that concentrated samples can be only measured in transmission geometry whilst dilute samples can be measured reliably in fluorescence.

**EXAFS data reduction**

There is a wide collection of reviews, papers, books and guides dealing with EXAFS data reduction (Beran and Libowtzky, 2004), here the basics of data reduction will be exposed in order to facilitate the reader a starting point to treat their data from the scratch. The EXAFS signal is a sum of waves due to the contribution of the neighboring atoms and the data reduction consists in extract the $\chi(k)$ from the raw absorption data. A Cu metal foil recorded at the Cu K edge is used as an example and the raw absorption spectrum is presented in Figure 9. The data reduction will allow us to derive structural parameters — number of neighbours, interatomic distances, Debye-Waller factor — at later stages of data analysis.

- **Step 1:** Consists in converting the measured intensities to $\mu(E)$ by applying eq. 1.
- **Step 2:** A smooth pre-edge function from $\mu(E)$ is subtracted to get rid of the background due to other absorption edges or instrumental noise by fitting a polynomial line to the spectrum below the edge.
- **Step 3:** The next step is to identify the threshold energy $E_0$ corresponding to the energy of the edge of the element of interest that typically is obtained from the energy of the maximum derivative of $\mu(E)$.
- **Step 4:** At this stage the $\mu(E)$ is normalized by the value corresponding to the approximated edge jump $\Delta\mu_0$.

- **Step 5:** Remove the post edge background with a function that simulates the absorption from an isolated atom. This step can induce error since a flexible function could match the whole $\mu(E)$ when we are only interested to remove the low frequency components of $\mu(E)$.
- **Step 6:** After the absorption edge has been background subtracted and normalized $\mu(E)$ is converted into $\mu(k)$ by applying eq. 3 and subsequently $\chi(k)$ is isolated from the absorption by applying eq. 2.
- **Step 7:** Finally since the $\chi(k)$ decays quickly to amplify the oscillations at high $k$ the EXAFS is $k$-weighted $k^n\chi(k)$ and Fourier transformed into R-space.

Data reduction is summarized in Figure 9 showing the 7 steps normally used in EXAFS data reduction in the standard EXAFS PySpline package.

**Data analysis**

The scattering amplitude and phase shifts of the $\chi(k)$ in eq. 4 can be calculated theoretically. The complete calculation is beyond the scope this treatment, however hints presented here will provide the major guidelines to the inexperienced reader to do it. The $\chi(k)$ function is reasonable easy to calculate using one of the different software packages (Beran and Libowtzky, 2004). Once these scattering factors have been calculated for a given structural model, they can be used in the EXAFS equation to refine structural parameters from our data. The functions $\delta(k)$, $f(k)$ and $\lambda(k)$ will be used in **eq. 4** to predict and modify the structural parameters $R$, $N$ and $\sigma^2$ and also allow $E_0$ change until the best fit for $\chi(k)$ is achieved.

Some considerations should be taken into account when performing data anaylisis regarding to the EXAFS resolution and the number of parameters available to refine.

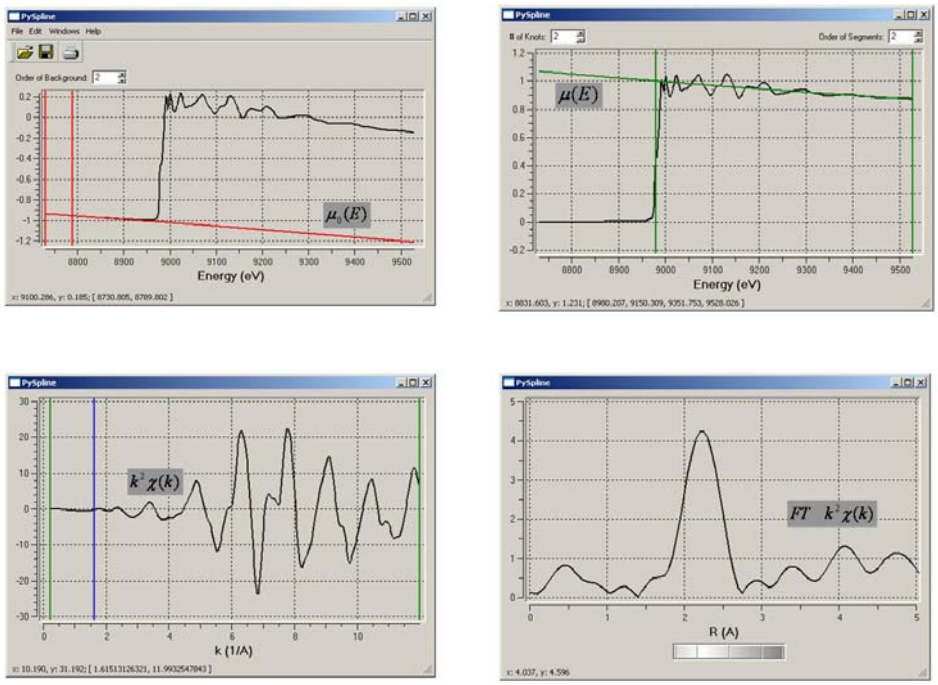


*Figure 9 Summary for a data reduction from for a Cu metal foil at Cu K-edge (a) fit of the pre-edge absorption curve (b) normalization of the spectrum (c) $k^2\chi(k)$ EXAFS signal in the metallic foil (d) and Fourier transform of the EXAFS showing the contributions of neighbors atoms.*

The resolution of EXAFS data can be calculated using the following relation

$$\Delta R \Delta k = 1 \quad \text{(eq. 5.)}$$

where $\Delta R$ corresponds to the spread of distances and $\Delta k = k_{\max} - k_{\min}$ is the data length. From eq. 5 can be concluded that and increase in $\Delta k$ induces a decrease in $\Delta R$ i.e. to resolve the distance spread of 0.1Å the data length should be $\Delta k > 10$ Å$^{-1}$. The number of degrees of freedom that correspond to the maximum number of parameters allowed to avay in a least square fit is given by the relation

$$N_{free} = \frac{2\Delta R_{fit}\Delta k}{\pi} \quad \text{(eq.6)}$$

according to eq.6 for a filtering window about 1Å and a data length $\Delta k$ of 12 Å$^{-1}$ the number of independent parameters that can be refined $N_{free}$ is 7.

$$R = \sum_i \left[ \frac{1}{\sigma_i} \left| Experiment(i) \right| - \left| Theory(i) \right| \right] \cdot 100\% \quad \text{(eq.7)}$$

where in eq.7 for a $k^3\chi(k)$ weighted EXAFS

$$\frac{1}{\sigma_i} = \left[k(i)\right]^3 / \sum_i \left[k(i)\right]^3 \cdot \left| Experiment(i) \right| \quad \text{(eq.8)}$$

A fit example for a Cu *K*-edge EXAFS is shown on Figure 10 with the calculated Cu-Cu distances for the coordination shells and angles for a typical Fm3m crystalline structure using EXCURV98 package. The obtained values are listed on Table 1 and compared to previous published data.

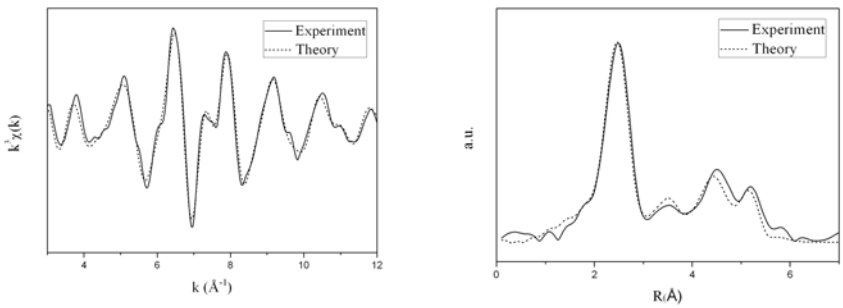


*Figure 10 (left) Cu-K edge EXAFS obtained on a Cu metal foil (a) EXAFS signal and (right) FT and fitting both showing the calculated fit in respect to the original data.*

During the fitting process more shells are included by simply adding another shell to the EXAFS sum and using calculated scattering factors for the Cu-Cu scattering. Accordingly the $R$, $N$ and $\sigma^2$ will be refined again and also the value of $E_0$.

The EXAFS analysis for a Cu metal foil can be quite straightforward, however real analysis can be much more complex with mixed coordination shells or effects from multiple-scattering in which the photo electron scatters from two or more atoms before returning to the absorbing atom.

| Copper foil | | | | | |
|---|---|---|---|---|---|
| Atomic | N | Dist | [a]Dist | $\sigma^2$ | R |
| Cu(1) | 12 | 2.54 | 2.556 | 0.018 | 22.1 |
| Cu(1) | 6 | 3.59 | 3.615 | 0.025 | |
| Cu(1) | 24 | 4.42 | 4.427 | 0.027 | |
| Cu(1) | 12 | 5.12 | 5.112 | 0.022 | |

*Table 1. EXAFS Cu K edge fittings obtained on metal foil. (N corresponds to the number of pairs of atoms, $\sigma^2$ to the Debye-Waller factor, R to the fit index. [a]Interatomic distances for Cu according to Wyckoff ,1963)*

**Applications in earth sciences and related disciplines**

Earth materials are often heterogeneous, and X-ray absorption fine structure techniques — EXAFS and XANES — combined with X-ray microprobes are shown to be valuable tools to elucidate their complexity, helping to provide information related to the speciation and local structure of the elements in relation with their hosting media.

The use of synchrotron techniques on a wide range of cultural heritage related problems has experienced an exponential growth in terms of the amount of scientific papers published since early 90's until the end of 2008, as shown on Pantos 2008. In parallel, the use of synchrotron radiation by different Spanish researchers on ancient objects attracted the attention of the media and have had and extended press coverage as

seen on Vendrell-Saz 2006. Nowadays there are several Spanish groups involved in research projects using synchrotron radiation on cultural heritage.

Synchrotron radiation — with its very high intensity, brightness, and energy tunability of X-rays — has allowed to perform element-specific spectroscopic studies of pollutants and trace elements in highly complex environmental samples and at highly diluted levels. These type of studies have led to unique information on many of the chemical processes that affect contaminant elements at the solid-water interface, and they have provided a great deal of basic data on the speciation and spatial distribution of toxic or economic interest chemical species in environmental samples.

*X-ray absorption applied on cultural heritage*

The understanding of cultural heritage objects involves an interdisciplinary collaboration between archaeology, art history, and preservation of the cultural heritage, ethnography and material science. Routinely any research starts with the characterization of the component materials and then some information can be extrapolated regarding the identification of its creative process, the evaluation of the alteration processes, the diagnosis of previous modifications and dating. — this information is extremely valuable to the conservator and restorers for preventive conservation and to the archaeologists to identify the provenance, manufacture and function of a wide range of objects. Third generation synchrotrons sources — thanks to beamlines with microfocussing capabilities that provide a high spatial resolution — fulfil most of the experimental needs to study cultural heritage samples which are heterogeneous and limited in nature i.e. standard painting cross sections have layers about 50-500 μm thick each containing pigments about 1-10 μm in diameter.

*Identification of the production process of lustre ceramics*

The understanding of how ancient objects were produced gives us the chance to understand how the past societies used and shared technologies giving us hints of their interaction and development. Ceramic pots and plates are one of the most significant physical remains since early stages of human civilizations and their study gives us the opportunity to elucidate the distribution, technological development and

connections amongst ancient societies. The ceramic production reached its maximum point of complexity and sophistication with lustre decorated ceramics — a ceramic decoration constituted by copper and silver nanocrstyals embedded inside a glassy matrix — that probably was developed in Irak during the 9th century and spread all across the western Mediterranean with the expansion of the Islamic culture. Spain had some of the most significant Islamic lustre ceramic production centers such as the archaeological sites from Paterna in the SE of Spain with important ceramic remains that have been extensively studied using synchrotron radiation techniques.

The study of lustre production from the *Olleries Xiques* archaeological site in the city of Paterna has been performed by using syncrhtron radiation based techniques.This site dates back from the 12th century and was an important district in Paterna densely populated of ceramic kilns exclusively dedicated to glazed ceramic production. During the 13th century the city was conquered by the Aragon Crown and occupied by the Christians, however the ceramic production did not stop and produced huge amounts of lead glazed ceramics decorated with lustre and was exported all across the Mediterranean. For their study and comparison ancient ceramic fragments on site were provided by the local archaeologists and modern lustre reproductions produced in the same way as their ancient ceramists counterparts had been obtained from a local workshop. These studies stated that copper and probably silver were introduced inside the glassy matrix by means of an ionic exchange between a raw paint and the alkalis from the glass during annealing in a reducing atmosphere Pradell et al. 2006 and Roque et al. 2006 and 2007.

The μ-XRF and μ-XANES/EXAFS in Figure 11 showed that aesthetic heterogeneities on the decorations correspond to silver and copper variations being copper and silver anticorrelated inside the glassy matrix in terms of chemical composition and oxidation state Smith et al 2006. Lustre final optical properties had been partly revealed as well by means of μ-XRD and TEM linking the accumulation and development of metallic nanoparticles inside the glass matrix to its characteristic shine and colour Roqué et al. 2006. By combining the microfocusing synchrotron radiation techniques with TEM microscopy and comparing the modern lustre productions with the archaeological ones it was found that the huge accumulation of

ceramic left over the *Olleries Xiques* site corresponded to defective productions with remarkable amounts of oxidized nanoparticles asthey provably did not fulfil the required aesthetic standards.

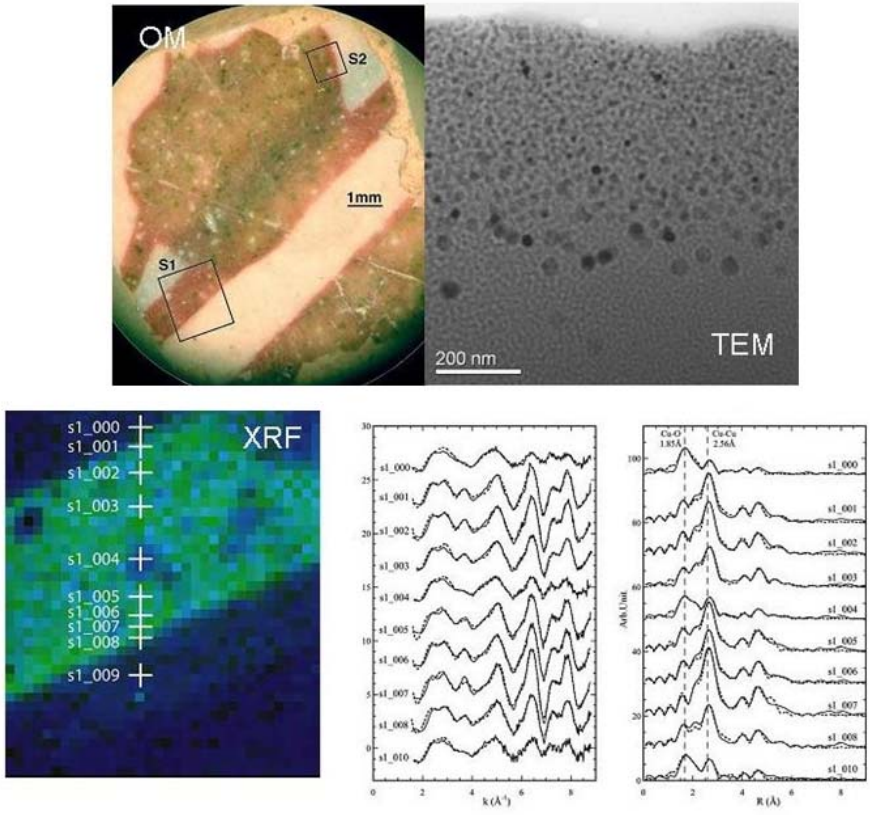


*Figure 11. Ceramic lustre from Paterna (Spain). Sampled region, TEM pictures showing copper nanoparticles, XRF mapping for Cu Ka, Cu K edge EXAFS spectra obtained across the lustre decoration and magnitude of the Fourier Transform of the EXAFS spectra.*

*Evaluation of the alteration processes in vermillion pigments.*

Environmental conditions have a significant effect on the appearance and properties of the objects constituting our cultural heritage. There are several examples

in the literature about applying microfocus synchrotron techniques to understand the weathering process occurring on art objects specially dealing with the darkening and fading of colours — these studies are generally focussed on either the changes affecting the binding media or the pigments — within the chromatic layers (Lluveras et al. 2000, Herrera et al. 2008; and Salvado et al. 2002). Other works are more orientated to the preservation of the structure of the objects themselves, this include examples regarding the study of corrosion processes occurring on metal pipes from Spanish baroque organs and the study of the acidification processes that take place in archaeological wood from sunk vessels (Herrera et al. 2009 and Wehterall et al. 2008).

The XAFS have been revealed as a set of powerful tools to identify vermillion pigments and the associated decay products within the chromatic layers. Vermillion is a cinnabar based pigment that has been used widely for paints and on a wide range of art objects. However some of the cinnabar resulted to be photosensitive and permanently blackens during a few hours of exposure to sunlight (*McCormack, 2000*). The cause of cinnabar photo-sensitivity has been suggested to be related to physical and chemical mechanisms — such as photo-oxidation — and changes in the crystalline structure (*McCormack, 2000; Cotte et al. 2006*). However some researchers suggested that most cinnabar is not sensitive to sunlight. Accurate analysis by means of electron microprobe and synchrotron radiation suggested that the content of halogens in cinnabar is related to the photosensitivity of the pigment (*McCormack, 2000; Cotte et al. 2006*). The main goal of the experiments is to track the presence of halogen elements in a wide range of ore minerals and pigments to try to link the presence of halogens in the mineral ores to their presence within the pigments themselves. This approach should help to elucidate if the darkening effect on pigments if mainly due to an exogenous process related to halogens reacting with the painting surface or if by the other hand corresponds to an autogenous process related to the halogens already present within the pigment composition.

A set of representative samples on Figure 12 corresponding to a wide range of cinnabars from the most important mercury sulphide ores from Europe, China and Japan jointly with other natural occurring mercury chloride have been studied. In parallel reagent mercury sulphide has been exposed into a 0.5M KCl solution after one

month in order to obtain some cinnabar samples with exogenous Cl. The mineral samples where mounted as cross sections with a metallographic polishing to map the distribution of the elements of interest. Pigment samples were available only in very small quantities and were mounted on top of Capton® tips. The mounting set up for the pigments allowed performing elemental mapping and XAS measurements on single grain particles focussing specifically on the pigment micron sized grains independently of the binding media and the other components from the chromatic layer.

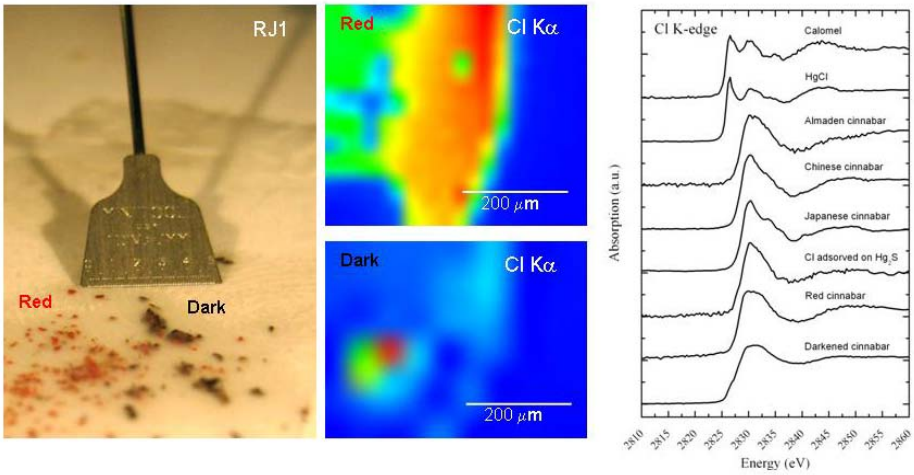


*Figure 12 On the left red and darkened pigment, on the centre Cl elemental distribution in non-darkened pigment and in darkened pigment and on the right Cl K-edge XANES on the darkened and non-darkened pigments compared to those obtained on selected minerals and the aged mercury sulphide reagent.*

The preliminary results show detected Cl on a wide range of natural cinnabars and on darkened and non-darkened pigments. The Cl distribution turned to be heterogeneous within the ore samples, located in very specific locations within the mineral. The Cl K-edge XANES performed on the cinnabar ores and on the pigment on Figure 12 showed a degree of similarity in their shape suggesting that the chemistry of Cl within the cinnabar minerals and within the pigment is probably somehow close related. The Cl K-edge XANES on the reagent mercury sulphide aged in the 0.5M KCl solution had a high degree of similarity with those obtained on both pigments and ores as well. However the Cl-K edge XANES from calomel $(HgCl)_2$ and $HgCl_2$ were

specific to these compounds and did not have any remarkable similarities with those obtained on the pigment and on the ores — it's worth to notice the development of a shoulder in the Cl K-edge XANES from the darkened cinnabar near the edge not present on the non darkened pigment as seen on Figure 12. It may suggest that the spectrum on the darkened cinnabar could be a combination of two or more Cl K-edge XANES.

**X-ray absorption applied on earth and environmental sciences**

The development of third generation synchrotron has benefited the environmental geochemistry and mineralogy research allowing to perform in situ studies of natural heterogeneous materials — soil, aqueous phases and poorly-ordered minerals — under near natural conditions. The recent developments in the applications of synchrotron based techniques allowed to improve the study of low-temperature environmental systems including biogeochemistry, geomicrobiology, soil science, carbon sequestration, metal and metalloid speciation studies in natural and contaminated environments, aqueous geochemistry, colloid science, nano particles, mineral/solution/bio interface studies, environmental radiochemistry and phytoremediation studies.

*Nickel in Moa Bay laterites*

The Caribbean holds ~10% of the global resources of lateritic Ni (Dalvi et al. 2004), and among them Cuba has the major deposits. The Cuban deposits are located at the NE of the island and are developed from serpentinized peridotites enclosed in Faja Ofiolitica Mayari-Baracoa (FOMB) (Proenza et al. 1999). These deposits are mainly oxides (Brand et al. 1998; Gleeson et al. 2003) and there are still questions about the different Mn and Ni bearing phases. In lateritic mineral deposits the materials rich in Mn and Ni are mainly amorphous or have low crystallinity but the ore also contains more crystalline haematites, maghemite, goethite and lithiophorite and intermediate products between asbolanes and lithiophorite. The low crystallinity and heterogeneity of laterites meant that is difficult to apply crystallographic tools to understand the development of the lateritic Ni mineral. To attempt to understand this system μ-XRF

and μ-XAS were used at the Ni K edge to evaluate the local environment of Ni. The study of Ni distribution and accumulation in the Moa Bay deposits provide a unique opportunity to understand the geochemistry of nickel on the earth surface — and potentially improve the Ni extraction processes from the ore minerals.

A polished sample corresponding to the limonitic horizon from the Moa Bay deposit was prepared and mapped using XRF with a resolution of 5 μm, illuminating with incident energy of 9.2 keV. The μXRF maps obtained on I18 demonstrate the high content of Mn and Ni in the micronodules and a matrix enriched with Fe as seen on the Mn, Fe and Ni map and an optical microscope image are shown in Figure 13(a). It is well known that these Mn micronodules show a great affinity with valuable transition elements such as Ni suggesting a chemical and structural relationship between Ni and Mn compounds. To obtain the spatial distribution of Cr, Mn, Fe, Co and Ni since the fluorescence lines Kb consecutively spills into the next Ka the XRF spectra have been fitted using the software package PyMCA from ESRF *(*Solé et al. 2007*)* and then the elemental map has been generated.

In the lateritic horizon much of the Ni is associated with the Mn phase. The Mn phase correspond to a layered structure constituted by stacked $MnO_6$ edge sharing octahedron with water molecules and/or metal cations in the interlayer region — some examples of such structres are the birnesites, lithiophorite and asbolane. One of the major mechanisms involved in metal accumulation in these phylomanganates is the surface complexation where metals bond to the surface by sharing one or several oxygen ligands with one or several Mn forming different types of complexes i.e. on $Mn^{+4}$ vacancies as triple corner or edge sharing or at layer edge as double corner sharing.

The collected XANES/EXAFS data Figure 13(b) at various points on the sample showed that the Ni speciation in the Mn-rich regions is close to $Ni^{+2}$ and preliminary EXAFS analysis using the EXCURV98 package (Binsted, 1996) suggested that most of the Ni is complexed on the surface of the Mn oyxhydroxides.

The Ni-Mn distances shown in Figure 13 (c) are 3.47 Å for the Ni rich region in red and 3.45 Å for the yellow region. These values are close to the 3.45 Å for Ni bidentate cluster adsorbed to the layered Mn as seen on Figure 13 (d) and thus

suggesting that most of the Ni is complexed rather than incorporated to the host mineral as seen in Peacock and Sherman, (2007) and Manceau et al. (2007). The Ni-Ni 3.03 Å and Ni-Al 3.08 Å distances corresponding to the asbolane cluster are also shown.

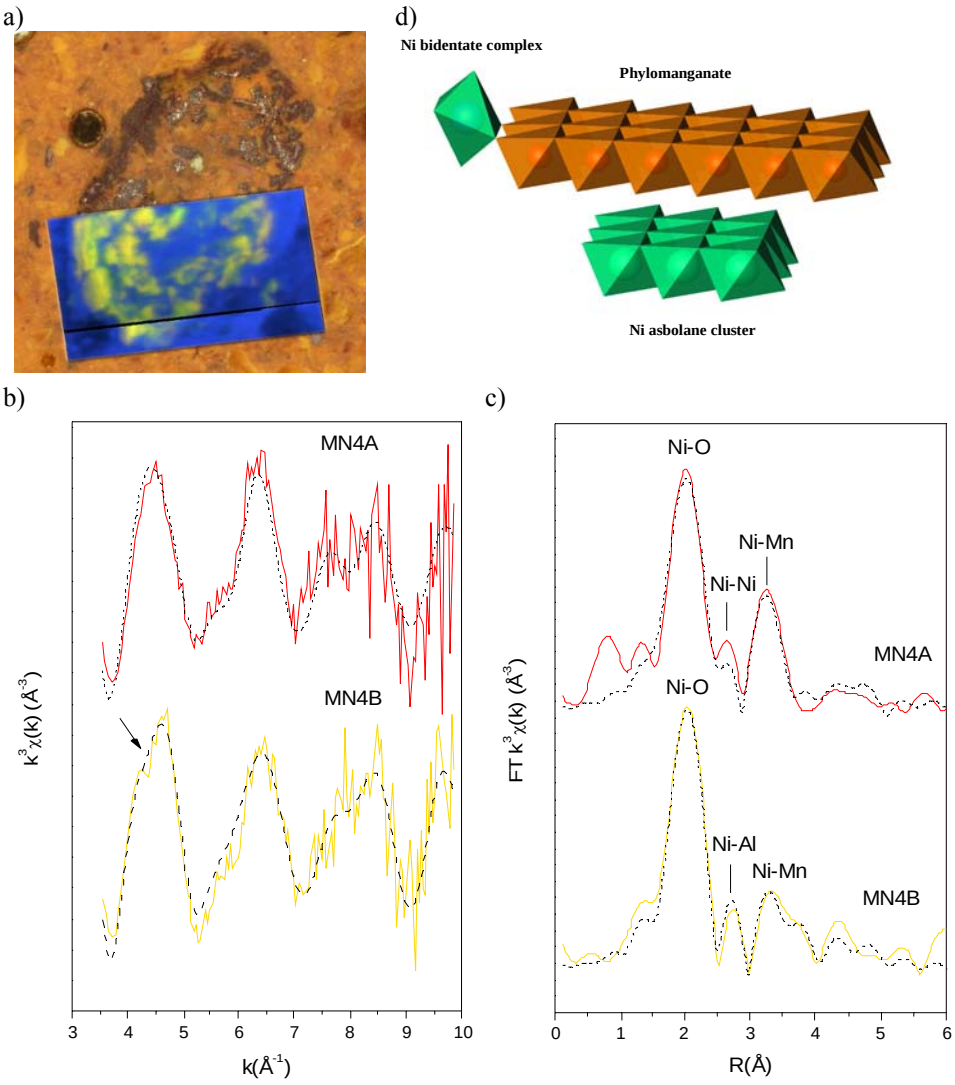


*Figure 13. (a)RGB XRF elemental map showing the distribution of Ni in red, Mn in green and Fe in blue (b) Ni K-edge k3 weighted EXAFS from yellow and red regions,(c) FT showing the radial distribution of the neighbouring elements (d) structural relationship of Ni with phylomanganates.*

**Conclusions**

A microfocus absorption spectroscopy beamline from low to middle energies, provides a full range of new experimental possibilities allowing achieving an ultimate understanding of the chemical and structural properties from minerals and art objects and has a huge potential in helping to elucidate a wide range of scientific cases. A microfocussing beamline is proved to be highly versatile and especially suitable for the sampling methodologies needed on a wide range of earth science related samples ranging from art objects, paintings and ancient ceramics to soil samples.

**References**

Beran A, Libowtzky Spectroscpy Methods in Mineralogy (2004) Eotvos University Press

Binsted, N. and Hasnain, S.S.(1996). J.Synch.Rad. 3,185

Brand, N.W., Butt, C.R.M. and Elias, M. (1998) Journal of Australian Geology and Geophysics, 17, 81-88.

Cotte M., Susini J., Metrich N., Moscato A., Gratziu C., Bertagnini A. and Pagano M. (2006) Analytical Chemistry 78, 7484-7492.

Dalvi, A.D., Bacon, W.C. and Osborne, R.C. (2004) Symposium on International Laterite Nickel 2004, Charlotte N.C., USA. 23-24.

Gleeson, S.A., Butt, C.R.M. and Elias, M. (2003) SEG Newsletter, 54, 11-18.

Herrera L.K., Cotte M., Jimenez de Haro M.C., Duran A., Justo A., Perez Rodriguez J.L., Applied Clay Science **42** (2008) 57-62.

Herrera L.K**,** Justo A., Sans J. A., Martínez-Criado G., Muñoz-Paez A. Trac Trend Anal Chem. (2009) submitted.

Howells, M.R., Cambie, D., Duarte, R.M., Irick, S., MacDowell, A.A., Padmore, H.A., Renner, T.R., Rah, S. and Sandler, R. (2000) Optical Engineering, 39, 2748-2762.

Lluveras A., Boularand S., Roqué J., Applied Physics A 2007 90(1) 23-33

Manceau, M. Lanson, N. Geoffroy (2007): Geochimica et Cosmochimica Acta 71 (2007) 95–128.

Martinez, C.E., Bazilevskaya, K.A. and Lanzirotti, A. (2006) Environmental Science and Technology, 40, 5688-5695.

McCormack, J. K. (2000) Mineralium Deposita 35, 796-798.

Mosselmans JFW, Quinn P D, Roque-Rosell J, Atkinson K D, Dent A J, Cavill S I, Hodson M E, Kirk C A and Schovield P F. (2008) Mineralogical Magazine 72 197–200.

Oliveira, S.M.B., Parititi, C.S. and Enzweiler, J. (2001). Journal of South American Earth Sciences, 14, 307-317.

Patrimoni-UB Recull de Premsa. [on line]. Barcelona, Spain: M. Vendrell-Saz, 29 May 2006 [Read: 18 March 2009]. Available: <http://161.116.85.21/patrimoniUB/>.

Peacock C. L. and Sherman D. M. (2007) *s* American Mineralogist 92, 1087-1092.

Proenza, J.A., Gervilla, F., Melgarejo, J.C. and Bodinier, J.L. (1999) Economic Geology, 94, 547-566.

Pradell T., Molera J. , Roque J., Vendrell-Saz M., Smith A. D., Pantos E. and Crespo D. *Ion-exchange mechanisms in the formation of medieval luster decorations* 2006 Journal of the American Ceramic Society **88**, 1281-1289.

SRS Daresbury. *(*2008) [on line]. Daresbury, UK: E. Pantos, 4Available: <http://srs.dl.ac.uk/arch/publications.html>.

Roqué J., Molera J., Sciau P., Pantos E. and Vendrell-Saz M.. Journal of the European Ceramic Society 2006 26(16) 3813-3824.

Roque J., Molera J., Perez-Arantegui J, Calabuig C., Portillo J, Vendrell-Saz M, 2007 Archaeometry **49** 511-52.

Salvadó N., Pradell T., Pantos E., Papiz M. Z., Molera J., Seco M. and Vendrell-Saz M. Journal of Synchrotron Radiation 2002 9 215-222

Solé V.A., Papillon E., Cotte M., Walter Ph., Susini J. (2007) Spectrochim. Acta Part B, 62 63-68.

Smith A.D., Pradell T., Roqué J., Molera J., Vendrell-Saz M., Dent A.J. and Pantos E. *y* Journal of Non-Crystalline Solids 2006 352 5353-5361

Wiedemann, H. (2003) Synchrotron Radiation. Springer, Berlin. 200

Wetherall K.M., Moss R.M., Jones A.M., Smith A.D., Skinner T., Pickup D.M., Goatham S.W., Chadwick A.V. and Newport R.J. Journal of Archaeological Sciences 2008 35(5) 1317-1328

Wyckoff R W G 1963 Crystal Structures vol 1 (New York: Interscience Publishers) p 7.